

# Plasmonic-Enhanced Cholesteric Films: Coassembling Anisotropic Gold Nanorods with Cellulose Nanocrystals

Zheng Cheng, Yi Ma, Lin Yang, Feng Cheng, Zhongjie Huang, Avi Natan, Hongyan Li, Yong Chen, Daxian Cao, Zhifeng Huang, YuHuang Wang, Yongmin Liu, Rendang Yang, and Hongli Zhu\*

**Incorporating photonic crystals with nanoplasmonic building blocks gives rise to novel optoelectronic properties that promise designing advanced multifunctional materials and electronics. Herein, the free-standing chiral plasmonic composite films are designed by coassembling anisotropic plasmonic gold nanorods (GNRs) and rod-like cellulose nanocrystals (CNCs). The effects of surface charge and concentration of the GNRs on the structure and optical properties of the CNC/GNR films are examined within this study. The CNC/GNR hybrid films retain the photonic characteristic of the CNCs host while concomitantly possessing the plasmonic resonance of GNRs. The negatively charged GNRs distribute uniformly in the layered CNCs host, inducing strong electrostatic repulsion among the CNCs and thus promoting the formation of a larger helical pitch than the case without GNRs. The positively charged GNRs decrease the chiroptical activity in the composite films with increasing the concentration of GNR, which is confirmed by the circular dichroism spectra. Notably, the surface plasmon resonances of GNRs enhance the fluorescence emission, which has been demonstrated by surface-enhanced fluorescence signals in this work. This study sheds light on fabricating functional chiral plasmonic composite films with enhanced chiral plasmonics by utilizing CNCs as a dynamic chiral nematic template and adjusting surface charges.**


Chiral plasmonic materials could offer the ability to achieve chiroptical-modulated activity over a wide spectrum region. However, achieving this has been a challenge in the chirality field for a long time.<sup>[1]</sup> Chiral plasmonic materials have many potential applications, including surface-enhanced signals (Raman, fluorescence, infrared absorption spectroscopy),<sup>[2]</sup>

circular polarizers,<sup>[3]</sup> plasmonic biosensors,<sup>[4]</sup> chiral catalysis,<sup>[5]</sup> and smart materials.<sup>[6]</sup> Additionally, functional guest species incorporated into a chiral nematic structured host offer new structures and properties to diversify chiral plasmonic materials. Metal nanoparticles (NPs) can support surface plasmons, which can confine light into sub-diffraction-limited region to greatly enhance light-matter interactions.<sup>[7]</sup> The effect of the collective oscillation of free electrons in metals due to the resonant coupling effect of electromagnetic waves is named as surface plasmon resonances (SPRs). SPRs' ability to regulate light properties at the nanometer scale has been widely explored over the past decades.<sup>[8]</sup> The resonances occur when metal NPs are illuminated by light at a certain frequency. And the resonant frequency is influenced by the species, morphology, dimension, and the surrounding dielectric environment.<sup>[9]</sup> Notably, shape-anisotropic metal NPs have the distinctive capability to concentrate the highest electromagnetic field on the edges.<sup>[10]</sup> The appealing plasmonic

shape-anisotropic gold nanorods (GNRs) display tunable surface plasmon resonances in the visible spectrum.<sup>[11]</sup> Compared with shape-isotropic metal NPs like spherical NPs, the shape-anisotropic plasmonic NRs possess excellent chiroptical activity by breaking the mirror symmetry, which is represented by circular dichroism (CD) characteristics. Therefore, the attractive

Z. Cheng, Y. Ma, A. Natan, Dr. H. Y. Li, Y. Chen, D. X. Cao, Prof. Y. M. Liu, Prof. H. L. Zhu  
Department of Mechanical and Industrial Engineering  
Northeastern University  
Boston, MA 02115, USA  
E-mail: h.zhu@neu.edu

Z. Cheng, Prof. R. D. Yang  
State Key Laboratory of Pulp and Paper Engineering  
South China University of Technology  
Guangzhou, CN 510640, China

 The ORCID identification number(s) for the author(s) of this article can be found under <https://doi.org/10.1002/adom.201801816>.

Dr. L. Yang, Dr. Z. F. Huang  
Department of Physics  
Hong Kong Baptist University (HKBU)  
Kowloon Tong  
Kowloon, Hong Kong SAR, China

F. Cheng, Prof. Y. M. Liu  
Department of Electrical and Computer Engineering  
Northeastern University  
Boston, MA 02115, USA

Dr. Z. F. Huang, Prof. Y. H. Wang  
Department of Chemistry and Biochemistry  
University of Maryland  
College Park, MD 20742, USA

DOI: 10.1002/adom.201801816

plasmonic NPs can be used for numerous fields, such as surface-enhanced Raman spectroscopy,<sup>[12]</sup> surface plasmon enhanced fluorescence,<sup>[13]</sup> nanoscale lasing,<sup>[14]</sup> and magneto-plasmonic sensing.<sup>[15]</sup> In particular, the unique nanostructures of noble metals could enhance the fluorescence signal from local fluorophores. This phenomenon is known as metal enhanced fluorescence (MEF), which has gained great attention recently.<sup>[16]</sup>

Liquid crystals have always been used as the well-defined structured template to pattern aligned metal NPs. The crystals create a polarization-dependent optical response.<sup>[17]</sup> Due to their localized surface plasmon resonances (LSPR), the integration of plasmonic NPs into the cellulose nanocrystals (CNCs) host is especially attractive.<sup>[18]</sup> The liquid crystals formed by CNCs have recently attracted considerable attention due to the intrinsic properties including abundant availability, renewability, rich surface chemistry, and superior mechanical property.<sup>[19]</sup> CNCs are highly crystalline, negatively charged, high-aspect-ratio rod-like NPs that can spontaneously self-assemble into chiral nematic liquid crystalline phases above a critical concentration.<sup>[20]</sup> As a result, the chiral nematic order is preserved in free-standing solid CNC films, in which adjacent CNC layers rotate counterclockwise with respect to each other and form a left-handed helical structure.<sup>[21]</sup> Consequently, the resulting CNC films are birefringent, iridescent and exhibit CD signal. The structure is sensitive to the polarization of light, that is, the CNC films selectively reflect the left-handed circularly polarized light.<sup>[22]</sup> Chiral nematic CNCs have been explored as a template for free-standing chiral nematic mesoporous films of silica, carbon, and titania for various applications.<sup>[23]</sup> Although it has been proved that CNCs can retain their ability to form chiral nematic structures in the presence of noble metal NPs,<sup>[24]</sup> the effects of plasmonic NPs on the structural and optical properties of resulting composite materials remain relatively unexplored. Additionally, direct use of CNC films as a host for the organization of differently charged GNRs to generate new CNC-based chiral plasmonic materials with enhanced chiroptical properties has not been reported.

Herein, we designed the soft matter composite films by co-assembling plasmonic GNRs with chiral nematic CNCs. The coupled optical properties between the photonic CNC host and plasmonic GNRs guest have been achieved. A detailed experimental investigation of the influences of surface charge and concentration of shape-isotropic plasmonic GNRs on the structural and optical properties of composite CNC-based films was conducted. As a whole, the negatively charged GNRs (n-GNRs) distribute uniformly in the layered CNCs host matrix, and cause strong electrostatic repulsion among CNCs to form a larger helical pitch than the counterpart without GNRs. The chiral nematic order of the CNCs preserved well in the solid film. However, the positively charged GNRs (p-GNRs) distribute randomly in the films, and the chiral nematic ordering of the CNCs composite film is disrupted due to the electrostatic interaction and particle flocculation. The concentration of GNRs in the composite film also affects the ability of the CNCs to organize into chiral nematic ordered regions. The CNC/n-GNR film retained strong chiroptical activity when the volume of  $4.0 \times 10^{-9}$  M n-GNR solution in the mixed suspension (GNR mixed with 5 mL of 3.0 wt% CNC) was below

4.0 mL. Whereas, the chiroptical intensity in CNC/p-GNR film decreased as the volume of p-GNR increases from 0 to 4.0 mL, which demonstrated the interruption of CD of the hybrid film. Nevertheless, both the CNC/n-GNR and CNC/p-GNR composite films exhibited surface-enhanced fluorescence (SEF) signals due to increased local electromagnetic fields and the plasmon coupling mechanism. The facile film preparation and superior characteristics of CNCs offer the multifunctional materials' development with value-added optical properties and other advantageous features such as sustainability and flexibility.

**Figure 1** illustrates the approach to prepare chiral plasmonic composite films, which is based on the evaporation-induced coassembly of CNCs and GNRs. After chemical and mechanical treatment of micro wood fiber from natural trees (Figure 1a), the cellulose fibers (Figure 1b) consisting of linear chains of ringed glucose molecules (Figure 1c) are obtained. Rich hydroxyl groups in cellulose molecules enable easy formation of intrachain and interchain hydrogen bonds. The amorphous regions of the cellulose microfibrils are selectively removed, and the crystalline regions of cellulose fibers are cleaved into nanocrystals with the acid hydrolysis process (Figure 1d).<sup>[25]</sup> Meanwhile, the negatively charged sulfate ester groups ( $-\text{OSO}_3^-$ ) are introduced onto the CNCs surface (Figure 1e). In this study, the chiral nematic structure is preserved in free-standing solid CNC films obtained by water evaporation from CNC and GNR mixed suspensions. This method for producing the films leads to the chiral assembly of the GNRs. The resultant films consist of layers of CNCs that rotate counterclockwise in the plane of the film, forming a left-handed helix. The GNRs are embedded into the chiral nematic scaffold of CNCs, as illustrated in Figure 1f,g. It is obvious that the different surface charge types of GNR affect the self-assembly property of the CNCs rods. More specifically, the n-GNRs orient parallel to the long axes of CNCs, and both n-GNRs and CNCs are perpendicular to the central axis of the left-handed helix forming the chiral plasmonic pattern. As a result, the chiral nematic order of the CNCs liquid crystal can be perfectly preserved and modified in the solid film with n-GNR (Figure 1h). By contrast, the addition of p-GNR leads to gelation of the CNC nanorods due to the electrostatic interaction and particle flocculation. Consequently, the p-GNRs distribute randomly in the layered CNCs matrix and the chiral nematic ordering of the CNCs composite film is disrupted (Figure 1i).

**Figure 2a** shows a 3.0 wt% CNC aqueous suspension (left), which was prepared from sulfuric acid hydrolysis. Due to the presence of sulfate ester groups on their surface, CNCs are negatively charged with an electrokinetic potential ( $\zeta$ -potential) of  $-40.5$  mV (Table S1, Supporting Information). The CNC dispersions are translucent blue (Figure S1, Supporting Information), and birefringence patterns are observed by crossed polarizers (Figure S2, Supporting Information). This confirms the substantial CNC polydispersity and anisotropic liquid crystal characteristic (Figure S3, Supporting Information).<sup>[26]</sup> In comparison, the GNR suspension (right) displays dark red color. The GNR is synthesized via a three-step seed-mediated growth process (Figure S4, Supporting Information). Dynamic light scattering (DLS) data shown in Figure 2b are used to evaluate the size distribution of CNCs and GNR. The CNCs have

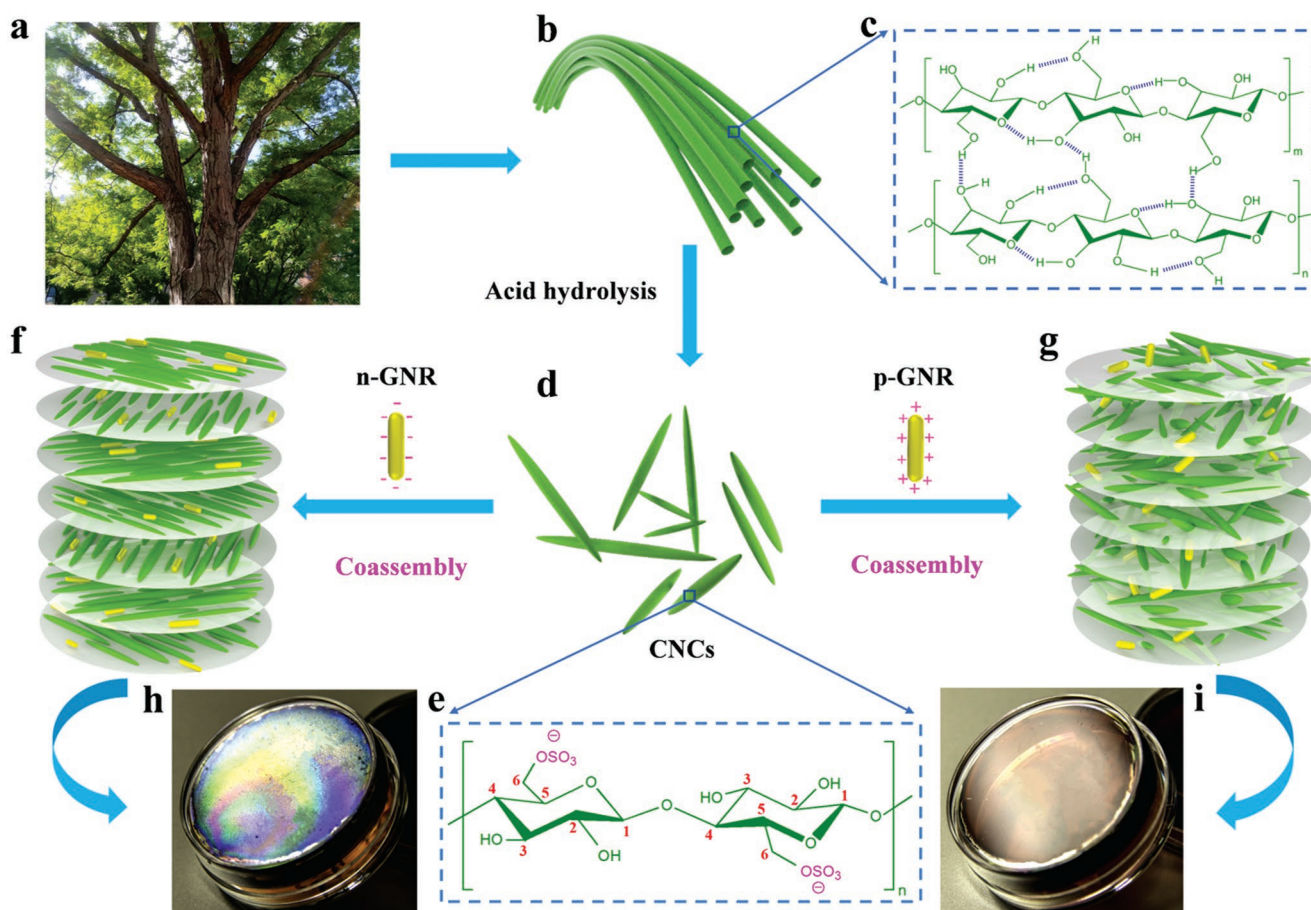


**Figure 1.** Schematic of the chiral plasmonic hybrid films prepared by mixing colloidal suspensions of CNCs and charged GNRs. a) Green trees. b) Cellulose fibers. c) The molecular structure of cellulose. d) Rod-like CNCs. e) The molecular structure of cellulose nanocrystal obtained from sulfuric acid hydrolysis, and the  $-\text{OSO}_3^-$  are introduced onto the surface of CNCs. f) The coassembly process of CNCs and n-GNRs. The n-GNRs distribute uniformly and align parallel to CNC rods. The chiral nematic order of the CNC liquid crystals are perfectly preserved. g) The coassembly process of CNCs and p-GNR. The p-GNR distributes randomly and forms partial agglomeration. The gelation and flocculation of the CNC nanorods are observed with some chiral nematic orders being disrupted. The obtained h) CNC/n-GNR hybrid film and i) CNC/p-GNR hybrid film at last.

average length of  $130 \pm 10$  nm, and the GNRs have an average length of  $40 \pm 10$  nm. The morphology and size of GNRs were further investigated by transmission electron microscopy (TEM) (Figure 2c). It is apparent that the rod-shaped gold nanoparticles have uniform dispersion and no aggregation of individual nanorods. Importantly, the p-GNR exhibits a positive value of  $\zeta$ -potential ( $+29.4$  mV), and the  $\zeta$ -potentials of the n-GNR is  $-46.8$  mV, which are confirmed by the zeta potential measurement (Table S1, Supporting Information). The CNC/ $x$ p(n)-GNR ( $x = 0, 0.5, 1, 2, 3$ , and 4) films were obtained from stable CNC/ $x$ p(n)-GNR mixed suspension during the correlative assembly, and the mixed suspensions were prepared by adding  $x$  mL of  $4.0 \times 10^{-9}$  M GNR solution to 5.0 mL of 3.0 wt% CNC aqueous suspension. The  $\zeta$ -potential of the CNC/ $x$ p(n)-GNR mixed suspension shows a different trend (Figure S5, Supporting Information). A high-magnification TEM image (Figure 2d) indicates that the monodisperse nanorods have a diameter, length, and aspect ratio of  $10 \pm 2$  nm,  $40 \pm 10$  nm, and  $4 \pm 1$ , respectively. Figure 2e is the typical TEM image of pure CNC, which is found to give stable aqueous suspensions of rod-like cellulose particles. After the addition of

polyethylene glycol (PEG), the CNC rods distribute more evenly (Figure S6a, Supporting Information). PEG acts as a depletion agent which helps to disperse the CNC rods, further explained by the excluded volume effect.<sup>[27]</sup> Different phenomena occur when the n-GNRs and p-GNRs are added into the CNC/PEG mixed suspension. The n-GNR disperses well in the CNC suspension due to the electrostatic repulsion (Figure S6b, Supporting Information), while the p-GNR forms flocculation phenomenon in the CNC suspension due to the presence of cationic species (both hexadecyltrimethylammonium bromide (CTAB)-coated NRs and free CTAB molecules) bridging with the CNCs (Figure S6c, Supporting Information).<sup>[11b]</sup> Figure 2f–h are photographs of the CNC suspension, CNC/n-GNR suspension, and CNC/p-GNR suspension, which are placed between crossed polarizers, and observed from a polarizer on one side. Figure 2f,g shows intense optical birefringence features, which is the characteristic feature of an anisotropic liquid crystal. Such birefringent patterns are stabilized due to negative charges on the surface of CNC (n-GNR). This confirms the absence of agglomeration as well as the preservation of the good self-assembly properties of CNC in suspension.<sup>[28]</sup> By

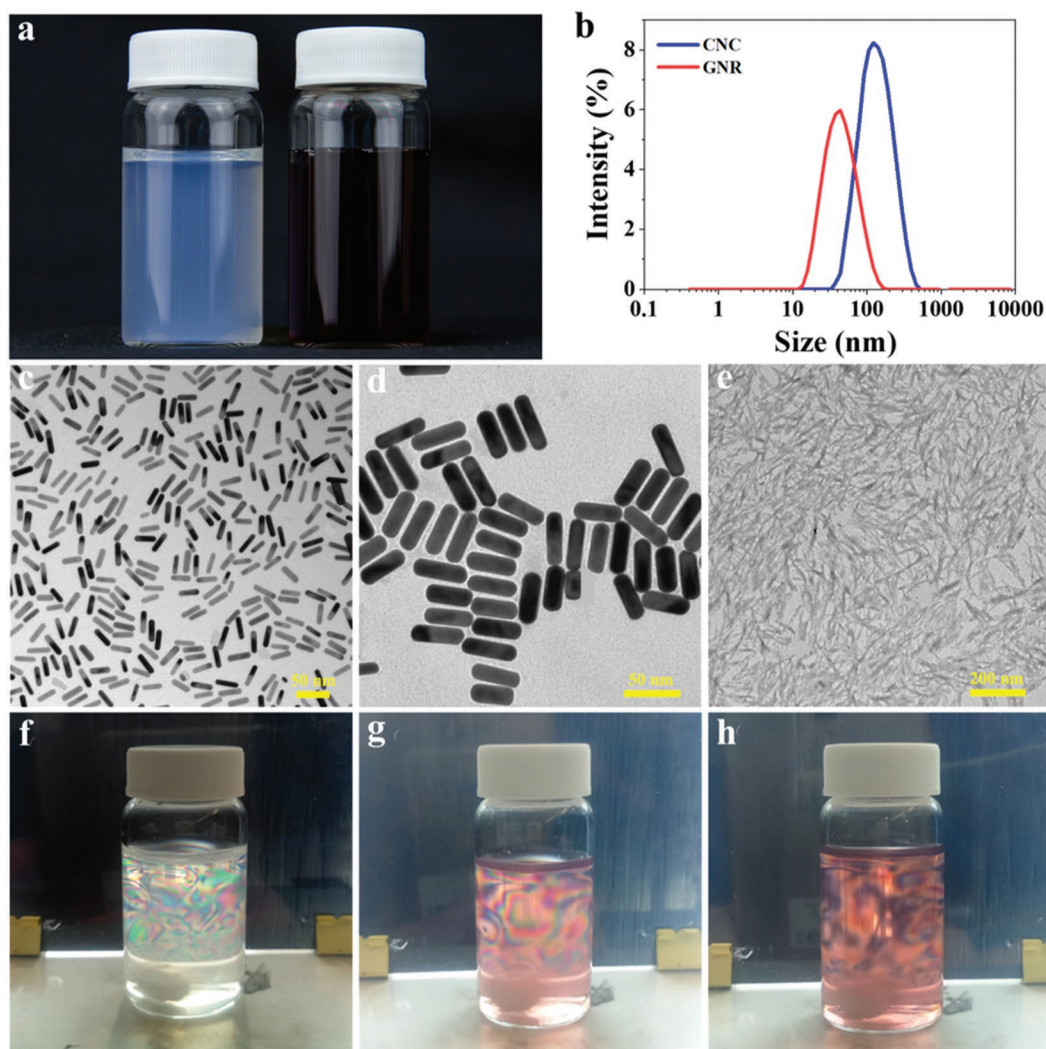


**Figure 2.** Characterization of CNC, GNR, and CNC/GNR aqueous suspension. a) Visual images of 3.0 wt% CNC suspensions (left) and  $4.0 \times 10^{-9}$  M gold nanorod suspensions (right). b) The DLS result shows the length distribution of CNC and nanorods. c) Low-magnification TEM image of gold nanorods. d) High-magnification TEM image of gold nanorods. e) CNC suspension observed by crossed polarizers. f) CNC/n-GNR mixed suspensions observed by crossed polarizers. g) CNC/p-GNR mixed suspensions observed by crossed polarizers. h) CNC/p-GNR mixed suspensions observed by crossed polarizers.

contrast, in the case of dispersion in a CNC/p-GNR solution (Figure 2h), the birefringence becomes blurry and flocculation. This confirms a charge interaction between the  $-\text{OSO}_3^-$  groups of CNCs and the p-GNR.

Four kinds of iridescent composite films with chiral nematic structure were prepared through slow evaporation of the water in the environmental chamber for 3 days at  $30^\circ\text{C}$  and humidity (RH) of 80% (Figures S7 and S8, Supporting Information). The pure CNC film shows a predominant color of blue with various iridescent color domains (Figure 3a), due to the random helix orientation of chiral nematic texture.<sup>[29]</sup> The solid pure CNC films exhibit photonic crystal properties and strong iridescent chiroptical activity (Figures S9 and S10, Supporting Information). Yellow is reflected by the CNC-PEG film mainly (Figure 3b) with a small red shift compared to the CNC film observed because of the steric stabilization induced by PEG. Interestingly, a large red shift is observed after addition of gold nanorod suspension. It is evident that the CNC/n-GNR

hybrid film has more uniform color and no agglomeration (Figure 3c), while the p-GNR has obvious agglomeration in the hybrid films (Figure 3d). The p-GNR will hinder the formation of chiral nematic structure of CNC due to their electrostatic interactions;<sup>[30]</sup> while the same concentration of n-GNR distributed uniformly inside the helical structure and further enhanced the chiral nematic structure. Polarized optical microscopy (POM) was used to investigate the microstructure of the composite CNC/GNR films at both low and high magnification. Strong birefringence and multidomains with random sizes and orientations are present in the pure CNC film due to the lack of control of helix orientation during evaporation (Figure 3e). The introduction of PEG shows no obvious effect on the appearance of birefringent and “finger-print” textures but a small change in the domain color (Figure 3f). The as-prepared CNC/GNR composite films show a progressive shift in the domain color from light green to dark red on the POM images. It is observed that the CNC/n-GNR hybrid film has

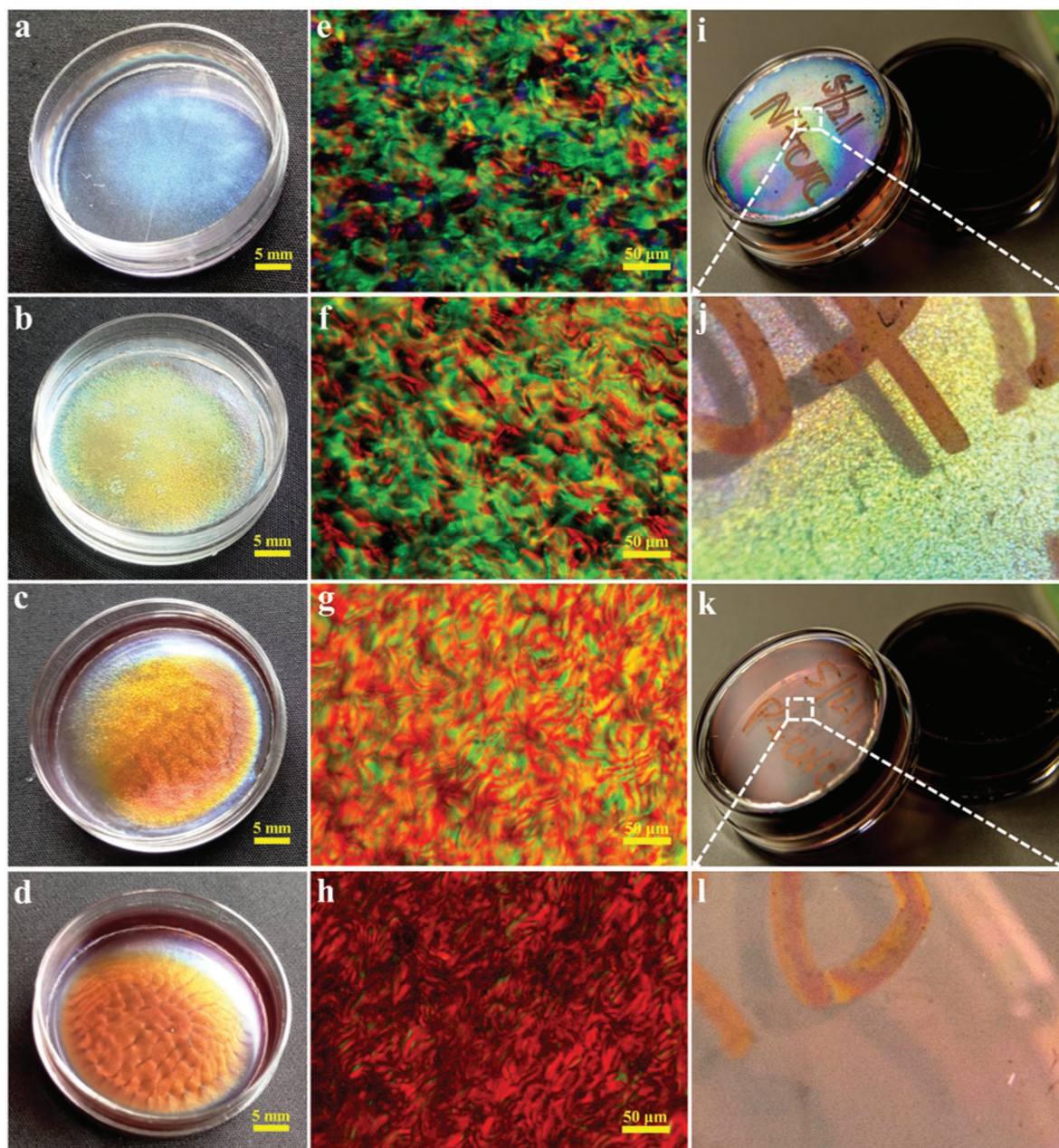


**Figure 3.** a–d) Photographs of pure CNC film, CNC/PEG film, CNC/n-GNR film, and CNC/p-GNR film. e–h) POM images of the surface of pure CNC film, CNC/PEG hybrid film, CNC/n-GNR hybrid film, and CNC/p-GNR hybrid film. i) Photograph of the surface of CNC/n-GNR (5.0 mL of 3.0 wt% CNC + 4.0 mL of  $4.0 \times 10^{-9}$  M n-GNR mixed suspensions) hybrid film, showing iridescent colors. j) Zoom in photograph of the surface of CNC/n-GNR hybrid film, showing granular fluorescent structure. k) Photograph of the surface of CNC/p-GNR (5.0 mL of 3.0 wt% CNC + 4.0 mL of  $4.0 \times 10^{-9}$  M p-GNR mixed suspensions) hybrid film. l) Zoom in photograph of the surface of CNC/p-GNR hybrid film.

more uniform iridescent color than the CNC/p-GNR film. Furthermore, the apparent fingerprint texture was observed by high-magnification POM (Figure S11, Supporting Information). The obvious planar texture (spaced parallel lines) indicates that the organized helical structures are persevered in the solid films.<sup>[31]</sup> It can be found that the fingerprint texture pattern of CNC/n-GNR hybrid film is neater and clearer than pure CNC and CNC/PEG films. The CNC/p-GNR film has a blurrier and less defined fingerprint texture pattern. Among the

four kinds of films (Figure S11a–d, Supporting Information), the space between two parallel lines in the long-range ordered fingerprint pattern of CNC/n-GNR hybrid film (Figure S11c, Supporting Information) is wider, indicating larger helical pitch inside the periodic layered structure. It demonstrates that the n-GNR increases the helical pitch by electrostatic repulsion with the negatively charged CNCs and does not disturb the formation of chiral nematic ordering. However, the agglomeration of the CNC/p-GNR hybrid films is observed due to

the presence of cationic species bridging the CNCs. The granular fluorescent structure of CNC/n-GNR hybrid film can be observed in high GNR concentration (Figure 3i,j), while that of CNC/p-GNR cannot even be observed in high GNR concentration (Figure 3k,l).

The chiral nematic structures of the CNC and CNC/GNR hybrid films were further examined by scanning electron microscopy (SEM). The SEM images of the cross-section of the CNC films give clear information about the periodic layered structure and the orientation of the CNCs (Figure 4a). An organized layered structure was further identified in the higher magnification in Figure 4b, and the long-range helical order was observed. In addition, the twisting is in the counterclockwise direction when the helical axis is viewed from above, thus it is in agreement with a left-handed helical organization.<sup>[25]</sup> The presence of the periodic layered structure is evident throughout the entire thickness, and the chiral nematic order is uniform and well-defined. After adding n-GNR, the cross-sections of the CNC/n-GNR hybrid films retain the periodic structure (Figure 4c). The compound films present the same characteristics of the chiral nematic arrangement in pure CNCs films. A higher resolution SEM image (Figure 4d) clearly shows n-GNRs appearing brightness on the CNC host, due to their higher surface electron density than the organic CNC matrix.<sup>[1b]</sup> The n-GNRs were dispersed uniformly and localized in the “parallel lines” which is the characteristic of the organization in CNCs layers. This suggests a similar alignment of the n-GNRs and CNCs in the hybrid material, which is induced by a spontaneous assembly of negatively charged gold nanorods into the CNC surface. Compared to the cross-section of CNC/n-GNR hybrid film, the CNC/p-GNR hybrid film still preserves a portion of the periodic structure although some disordered regions do occur in the films (Figure 4e). The random aggregation of p-GNR inside the surface plane of CNC is apparent in the SEM image (Figure 4f) with higher magnification, which can be attributed to partial cationic species bridging with the CNC rods. In addition, the homogeneous distribution of n-GNR is observed on the surface of CNC/n-GNR film, whereas the flocculation occurs on the CNC/p-GNR film (Figure S12, Supporting Information).

Integrating plasmonic gold nanoblocks with a chiral nematic structured CNC leads to chiral nematic films of CNC/GNR. These films show an optical response associated with the chiral assembly of GNR and strong plasmonic optical property. The fluorescence emission (under 365 nm light) peak of the CNC/GNR films shows GNR concentration-dependent fluorescence intensity, and the SEF signals are observed. MEF is a phenomenon that arises due to LSPR. A schematic illustrating the basic working principle of MEF is shown in Figure 5a. The observed enhancement of fluorescence is ascribed to an increase of excitation rate in the case of resonant excitation of surface plasmons, which depends directly on the intensity and the square of the local electromagnetic field.<sup>[11,32]</sup> Observation shows that both CNC/n-GNR and CNC/p-GNR generate an intense fluorescence centered at about 525 nm. Notably, increasing n-GNR loading markedly increases the peak intensity (Figure 5b), while increasing the loading of p-GNR shows the opposite trend (Figure 5c). This is because the n-GNR

distributed uniformly inside the helical structure. The GNR can interact strongly with light due to their ability to support surface plasmons, thus significantly enhancing fluorescence signals.<sup>[16a,33]</sup> While increasing the concentration of p-GNR will cause more agglomeration, which will cause greater energy loss and impede to the optical signal enhancement.<sup>[23a]</sup> Chiral fluorescent composite films of gold nanorods and photonic cellulose nanocrystals demonstrate modulated fluorescence emission due to the plasmonic–photonic coupling effect between the photonic CNCs and fluorescent GNR. A photograph of CNC/GNR hybrid films further shows tunable iridescent colors (Figure 5d). As n-GNR ratio is increased there is an increase in fluorescent color intensity. Whereas there is a decrease in fluorescent color intensity with increasing p-GNR ratio. The CNC/n-GNR hybrid films have an excellent chiral arrangement in high n-GNR concentration, while the CNC/p-GNR's chiral features cannot be observed in high p-GNR concentration.

The optical properties of the composite films can be tuned by changing the surface charge and concentration of GNR. The pure CNC films exhibit a reflectance peak of 400 nm (Figure S13, Supporting Information), which is the characteristic of the photonic crystals resulting from the CNC organization in a chiral nematic structure.<sup>[30]</sup> The reflectance peak  $\lambda_{\text{max}}$  shifts to 460 nm after addition of the PEG (CNC/PEG = 9:1, w/w). The optical properties of the prepared films (CNC/n-GNR, CNC/p-GNR) display both characteristics of longitudinal and transversal localized surface plasmon resonance (LLSPR and TLSPR, respectively).<sup>[34]</sup> The characteristic TLSPR band of CNC/p-GNR hybrid films resembles those of the CNC/n-GNR hybrid films at 520 nm, and the LLSPR band of CNC/n-GNR hybrid films (located at a wavelength of roughly 810 nm, Figure 5e) exhibits a red-shift compared to that of the CNC/p-GNR hybrid films (located at roughly 750 nm, Figure 5f). The transmittance of CNC/n-GNR hybrid films decreases with the volume of n-GNR increasing. The UV–vis spectrum is sensitive to the shape and aggregation states of the GNRs, as a result, the shift or change in the position of the plasmon bands would occur.<sup>[35]</sup> The UV–vis spectrum of CNC/n-GNR hybrid film shows a small red-shift of the LLSPR band. Since the polymer coating of GNRs will change the local refractive index, the small red-shift also supports the successful layer by layer coating of GNRs with charged poly(sodium-p-styrenesulfonate). No significant change in the spectral position of the n-GNR plasmonic bands occurred with an increasing n-GNR content in the films (Figure 5e). The intensity of the bands decreased with increasing GNR content in the films, and the intensity remains unchanged after the volume of GNR in the suspension reaching 4.0 mL. It is worth noting that the weak signature of the stop band (460 nm) appears on the left side of the TLSPR peak of CNC/n-GNR hybrid films, corresponding to the photonic bandgap of the CNC matrix. However, the TLSPR peak overlapped with the stop band of the CNC host in the CNC/p-GNR hybrid films (Figure 5f). A small blue-shift of the characteristic TLSPR band of CNC/p-GNR hybrid films occurred with an increasing p-GNR content in the films, which is due to the p-GNR aggregation and the partial loss of anisotropy in the CNC matrix, consistent with the TEM image of CNC/p-GNR mixed solution.

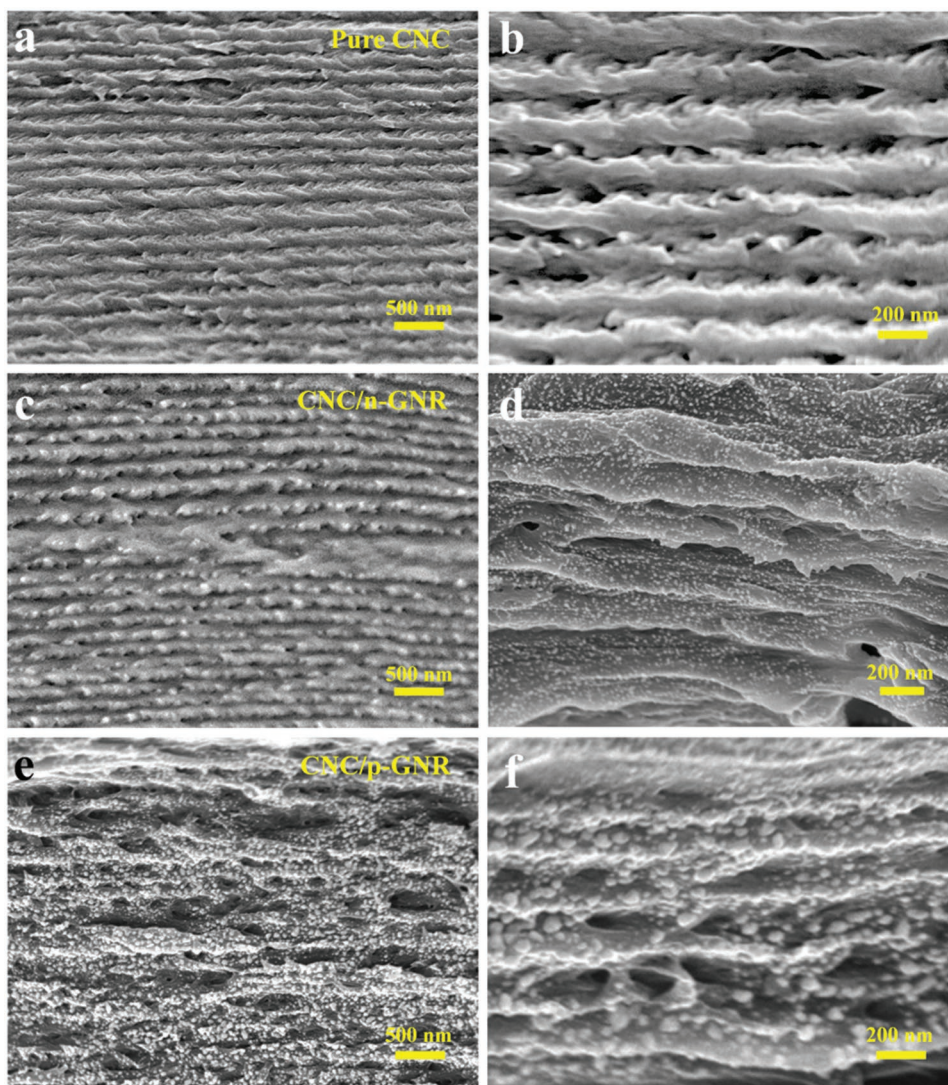


**Figure 4.** SEM cross-section images: a,c,e) Low-magnification images. b,d,f) High-magnification images. a,b) The pure CNC films. c,d) CNC/n-GNR hybrid films (5.0 mL of 3.0 wt% CNC + 2.0 mL of  $4.0 \times 10^{-9}$  M n-GNR mixed suspensions). e,f) CNC/p-GNR hybrid films (5.0 mL of 3.0 wt% CNC + 2.0 mL of  $4.0 \times 10^{-9}$  M p-GNR mixed suspensions).

Chiral cellulose films are capable of separating incident light into circularly polarized light (CPL) with opposite helicity states by selective reflection and transmission caused by its left-handed helical structure.<sup>[36]</sup> Figure 6a illustrates the inherent ability of the chiral cellulose materials to transform incident light into passive left-handed CPL (L-CPL) by the selective reflection and into passive right-handed CPL (R-CPL) by the transmission. The difference in the absorption of L-CPL and R-CPL is observable. The CD spectra of the CNC/GNR hybrid films exhibit a strong positive CD peak, a typical left-handed chiral characteristic, which is associated with the chiral nematic structures inside the CNC/GNR hybrid films.<sup>[3]</sup> CD is defined as the difference in extinction of left- and right-handed circularly polarized light

$$\begin{aligned} \text{CD} &= \text{Ext}_{\text{LCP}} - \text{Ext}_{\text{RCP}} \\ &= (I_{\text{LCP}} - T_{\text{LCP}}) - (I_{\text{RCP}} - T_{\text{RCP}}) \\ &= T_{\text{RCP}} - T_{\text{LCP}} \end{aligned} \quad (1)$$

Here  $\text{Ext}_{\text{LCP}}$  and  $\text{Ext}_{\text{RCP}}$  denote the extinctions of L-CPL and R-CPL, respectively.  $I_{\text{LCP}}$  and  $I_{\text{RCP}}$  represent the intensities of L-CPL and R-CPL, respectively, and  $I_{\text{LCP}} = I_{\text{RCP}}$ .  $T_{\text{LCP}}$  and  $T_{\text{RCP}}$  represent the transmissions of L-CPL and R-CPL, respectively.

The CD signals of the CNC/GNR hybrid film are associated with the chiral nematic order, and poor chiral nematic order weakens the optical activity of the hybrid film. It is observed in Figure 6b that the increase of the n-GNR volume from 0.5 to 3.0 mL leads to an evident redshift of the CNC's CD peaks, due to an increase of dielectric constant of the GNR-related surrounding medium of the CNC/n-GNR hybrid films,<sup>[37]</sup> and causes nearly no change in the CD peak intensity, indicating the well-kept chiral order of the hybrid films. However, increasing the p-GNR volume from 0.5 to 3.0 mL causes not only the CD redshift but also the marked decrease (Figure 6c), and the CD weakening can be ascribed to the lower fraction of the regions with a chiral nematic structure in the films with a higher

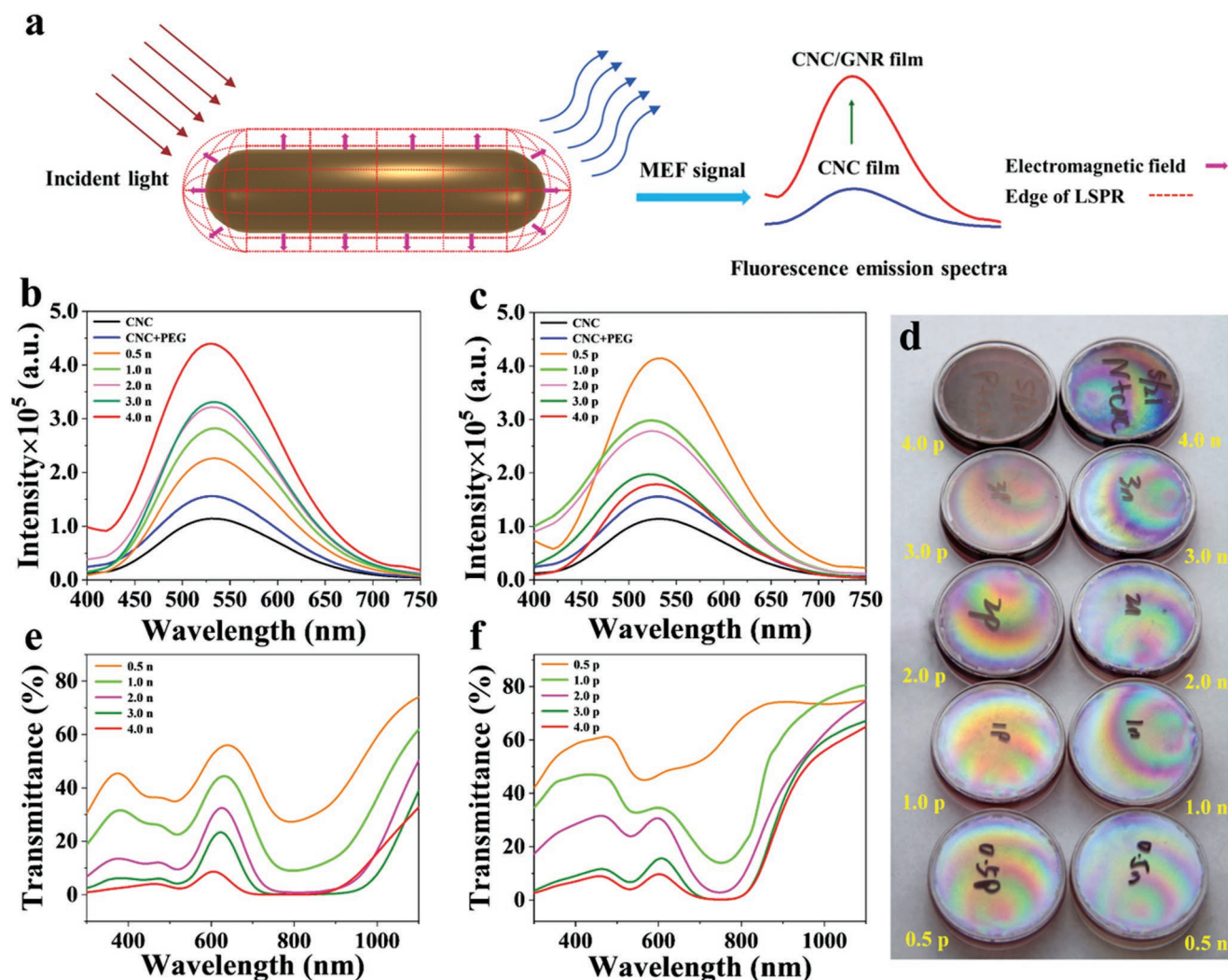


**Figure 5.** Optical characterization of CNC/GNR hybrid films with varying GNR loading. a) Schematic diagram illustrating the mechanism of MEF. The red and blue arrows near the GNR surface represent incident light and MEF signal, respectively. The MEF signal in the CNC/GNR hybrid films significantly enhances compared to that of pure CNC films. b) Fluorescence emission spectra showing that the peak intensity increases with increasing n-GNR loading. c) Fluorescence emission spectra showing that the peak intensity decreases with increasing p-GNR loading. d) Photograph of CNC/GNR hybrid films, showing tunable iridescent colors. There is an increase in fluorescent color intensity with increasing n-GNR ratio (right column) and a decrease in fluorescent color intensity with increasing p-GNR ratio (left column). The CNC/n-GNR hybrid films have good chiral arrangement in high n-GNR concentration. Whereas, the CNC/p-GNR's chiral features cannot be observed in high p-GNR concentration. e) UV-vis spectra of the CNC/n-GNR hybrid films prepared from different concentration of n-GNRs. f) UV-vis spectra of the CNC/p-GNR hybrid films prepared from different concentration of p-GNRs.

concentration of GNR. When the volume of GNR reaches 4.0 mL, both CNC/n-GNR hybrid film and the CNC/p-GNR hybrid film exhibit weaker intensity of the CD peaks. And the addition of 4.0 mL GNR makes the optical activity change from a single, positive CD peak to a pair of bisignate CD peaks (including positive and negative CD peaks) (Figure 6d,e). Large GNR aggregates are observed on the surface of CNC matrix are observed (Figure S14, Supporting Information). The heavy loading of n- and p-GNR tends to destruct the parallelly layered nanostructures of the hybrid films, accounting for the CD weakening. At 3.0 mL of GNR, the CD peak of CNC/n-GNR hybrid film is located at 670 nm and CNC/p-GNR hybrid film at 600 nm. It is obvious that the CNC and GNR may self-organize forming a host-guest composite film via repulsive interactions,

and the stabilized distribution of GNRs in the composite film is determined and stabilized by the repulsive interactions between the negatively charged host and the guest species when the volume of the GNR solution is below 3.0 mL. Attempts to further increase GNR loading resulted in a random aggregation of CNC/GNR with little chiral nematic ordering. This effect further supports differently charged plasmonic GNRs contribution to different chiroptical activity of the composite films. It is still ambiguous the reason that the addition of 4.0 mL GNR gives rise to the bisignate CD peaks, which is likely induced by GNRs. Even so, the chiral plasmonic CNC/GNR hybrid material exhibits tunable chiroptical characteristics.

In conclusion, we have developed free-standing chiral plasmonic films by coassembly of rod-like CNCs and anisotropic



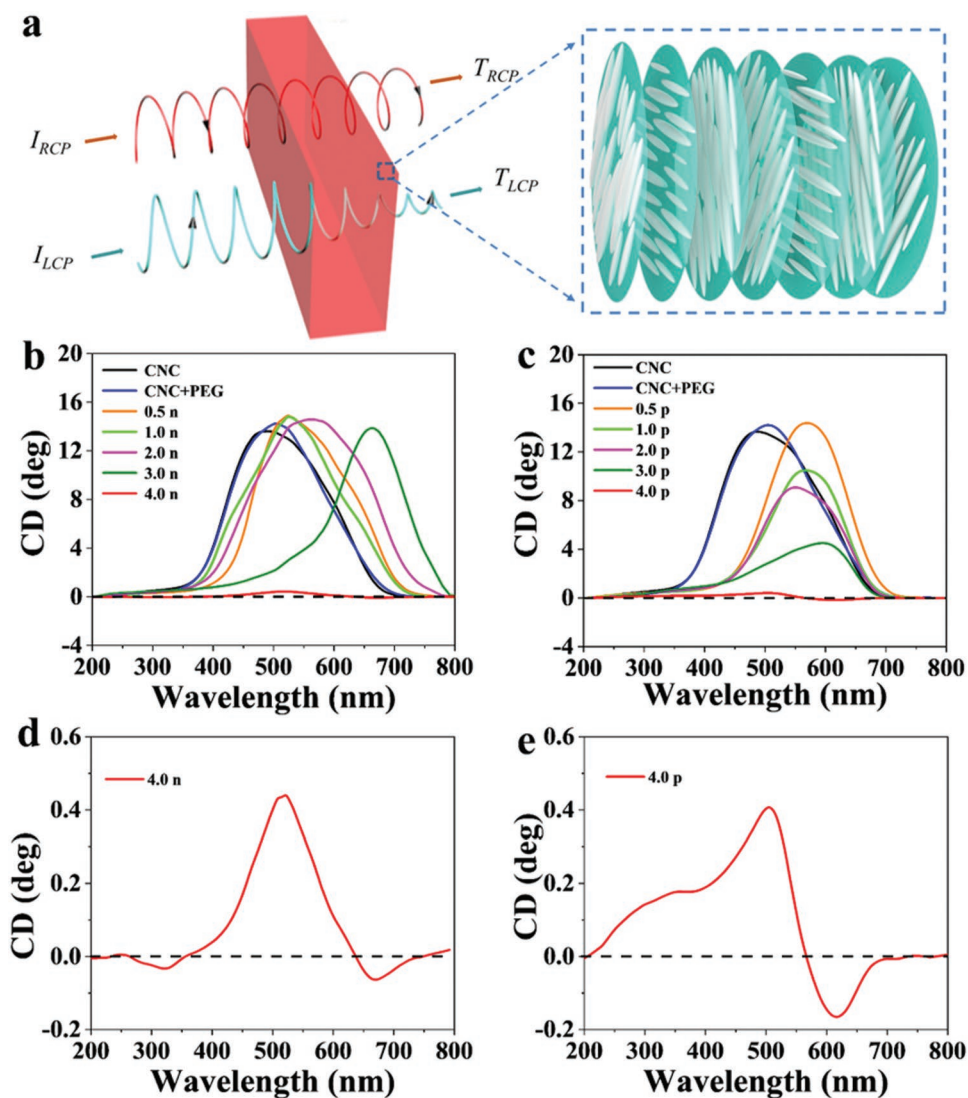


**Figure 6.** Chiroptical activity of the CNC/GNR hybrid films. a) Schematic illustration of the circularly polarized light passing through the left-handed chiral structured CNC film material. The chiral photonic film transforms incident light to passive left-handed circularly polarized light by the selective reflection and to passive right-handed circularly polarized light by the transmission. b) CD spectra of the CNC/n-GNR hybrid films. c) CD spectra of the CNC/p-GNR hybrid films. d) Zoom in CD spectra of CNC/n-GNR (4.0 mL n-GNRs) hybrid films. e) Zoom in CD spectra of CNC/p-GNR (4.0 mL p-GNRs) hybrid films. The CD spectra of the CNC/GNR films show the tunability in left-handed organization and intense plasmon modified chiroptical activity of the embedded GNRs.

GNRs. The GNR guests with different surface charges and various concentrations were embedded into chiral nematic CNCs matrix to form macroscopic CNC/GNR hybrid films. The host-guest hybrid films exhibit tunable plasmonic optical properties including surface-enhanced fluorescence and plasmon-modified chiroptical activity. The interesting properties of the films originate from the interaction of the photonic properties of the CNC matrix and plasmonic characteristics of GNRs. The n-GNRs induce strong electrostatic repulsion with the CNCs and thus promote the formation of a larger helical pitch with good chiral nematic order, while the chiral nematic order of CNC/p-GNRs is disrupted by the opposite charges. This study demonstrates the chiral nematic films coassembled with nanoplasmonic building blocks, which is applicable to the development of advanced functional optoelectronics

with tunable plasmonic properties. The composite chiral plasmonic material exhibited surface-enhanced fluorescence and tunable chiroptical characteristics. These characteristics are beneficial for fundamental studies of plasmonic optical properties and have diverse potential applications in optical imaging, biosensors, etc.

## Experimental Section

**Materials:** Microcrystalline cellulose (MCC) was purchased from Sigma-Aldrich Co. Ltd. Sulfuric acid (98 wt%) and dialysis tubes were purchased from Fisher Scientific. Tetrachloroauric (III) acid trihydrate (99.99 wt%), NaBH<sub>4</sub> (98.0 wt%), and L-ascorbic acid (≥99.0 wt%) were purchased from Fisher Scientific; AgNO<sub>3</sub> (≥99.0 wt%), CTAB (≥99.0 wt%), PEG (*M<sub>w</sub>* = 20 kDa), and poly(sodium-p-styrenesulfonate)

(PSS,  $M_w = 70\,000\text{ g mol}^{-1}$ ) were purchased from Sigma. All other chemicals were of analytical grade and used as received without further purification.

**Preparation of CNC:** CNCs were obtained by sulfuric acid-catalyzed hydrolysis method.<sup>[38]</sup> Concretely, MCC was added to 64 wt% sulfuric acid (1:10, w/v) under constant mechanical stirring at 45 °C for 45 min. The reaction was quenched by dilution with an excess of water. The suspensions were washed with deionized water through repeated centrifugation. At last, the resulting precipitate was dialyzed with deionized water using dialysis tubes until the pH of the water remained constant. The samples were sonicated and then stored in the refrigerator at 4 °C for further use.

**For Gold Seed Preparation:** 10.0 mL of  $200 \times 10^{-3}\text{ M}$  CTAB aqueous solution and 10.0 mL of  $0.5 \times 10^{-3}\text{ M}$   $\text{HAuCl}_4$  were mixed together. Then 6.0 mL of ice-cold  $10 \times 10^{-3}\text{ M}$   $\text{NaBH}_4$  was added while stirring. The mixture, which turned into a brownish-yellow solution indicating formation of small gold seed particles, was used as the seed solution within 5 min after preparation.<sup>[39]</sup>

**For Growth Solution Preparation:** 100 mL of  $200 \times 10^{-3}\text{ M}$  CTAB solution and 5.0 mL of  $4 \times 10^{-3}\text{ M}$   $\text{AgNO}_3$  solution were mixed. 10.0 mL of  $10 \times 10^{-3}\text{ M}$   $\text{HAuCl}_4$  and 80.0 mL of additional  $\text{H}_2\text{O}$  were added into this mixture. After gentle mixing, 500  $\mu\text{L}$  of  $200 \times 10^{-3}\text{ M}$  freshly prepared ascorbic acid solution was added.<sup>[35a]</sup>

**For Gold Nanorod Production:** Three test tubes (labeled A, B, and C), each contain the growth solution of volume above. Next, 1.0 mL of the seed solution was mixed with solution A. 1.0 mL of solution A was transferred to B after 15 s of seed to A, and 1.0 mL of solution B was transferred to C after 30 s of adding solution A to B. This solution was kept at a constant temperature of 28 °C for 48 h to complete the reaction.<sup>[40]</sup>

To purify and concentrate the gold nanorods, the as-prepared GNR solution was centrifuged at 12 500 rpm for 15 min to remove the excess amount of CTAB, which was followed by redispersion in  $\text{H}_2\text{O}$ , defined as p-GNR stock solution.

**Preparation of Negatively Charged Gold Nanorod:** First, 1.0 mL of the centrifuged GNRs solution was mixed with 500  $\mu\text{L}$  of PSS stock solution ( $10\text{ mg mL}^{-1}$ ). After 60 min of adsorption time, the PSS-coated GNR solution was centrifuged and washed two times to remove the excess amount of PSS and redispersed in deionized water, resulting in n-GNR stock solution.<sup>[41]</sup>

**Preparation of CNC/GNR Hybrid Films:** A desired amount of 8.0 wt% aqueous solution of PEG was added to the 5.0 mL of 3.0 wt% neutral CNC suspension ( $m_{\text{PEG}}:m_{\text{CNC}} = 1:9$ ) by vigorous stirring. Then different volumes (0, 0.5, 1.0, 2.0, 3.0, and 4.0 mL) of as-prepared p-GNR and n-GNR ( $4.0 \times 10^{-9}\text{ M}$ ) solutions were added to the mixed suspensions, respectively. And the mixtures were stirred at room temperature for 30 min and then sonicated in an ice bath to obtain a homogeneous mixture. Then the mixture suspension was drop-casted into a 35 mm diameter polystyrene petri dish and allowed to evaporate at ambient conditions (30 °C, 80% RH) for 72 h to give rise to free-standing iridescent chiral nematic CNC/GNR hybrid films. The obtained films were defined as CNC/ $x\text{p}(n)$ -GNR ( $x = 0, 0.5, 1.0, 2.0, 3.0, 4.0$ ). Finally the films were peeled off from the petri dish for characterization.

**Zeta Potential Test:** The 0.1 wt% CNC suspension was prepared, and the zeta potential of the CNC suspension was measured at 25 °C using a zeta potential analyzer (HORIBA SZ-100, Japan). The reported zeta potential was averaged from the results of five measurements.

**DLS:** Dynamic light scattering was used to determine the hydrodynamic diameter of CNC suspensions using a particle size analyzer (HORIBA SZ-100, Japan). CNC suspensions were diluted to 0.01 wt% in advance. Each sample was replicated three times to obtain the averaged hydrodynamic diameter.

**Transmission Electron Microscopy:** A small droplet of the diluted CNC suspension was deposited on a 300 mesh copper grid coated with carbon film. The excess liquid was absorbed by filter paper after 1 min. Subsequently, the TEM images were obtained by using a JEM-1010 transmission electron microscopy (JEOL, Japan) at an accelerating voltage of 80 kV.

**Polarized Optical Microscopy:** A home-built polarized optical microscopy device was used to determine the cholesteric pitch of the liquid crystalline phase in the CNC films. The films were cut into pieces and placed directly on glass slides.

**UV-Vis Spectrum:** Transmission spectra of the freestanding films at 300–1100 nm wavelength were measured using a PerkinElmer Lambda 1050 UV-vis-NIR spectrophotometer equipped with a 150 mm integrating sphere.

**Scanning Electron Microscopy:** SEM (S3700 Hitachi Ltd. Japan) was used to examine the morphology of the liquid crystal films. The cross-section of the films was obtained by fracturing the sample in liquid nitrogen and then fixing it to a metal-base specimen holder using double-sided tape. The fixed samples were coated with a layer of  $\approx 30\text{ \AA}$  thick of gold or palladium. The accelerating voltage was 10 kV and the working distance was 11 mm.

**Fluorescence Emission Spectrum:** Photoluminescence spectra of the films were recorded on a NanoLog spectrofluorometer (HORIBA Jobin Yvon), with the excitation light wavelength of 365 nm.

**Circular Dichroism Spectrum:** Circular dichroism spectra were monitored in transmission mode (Olis 1000 CD), under circularly polarized incident light. A sample was rotated clockwise at 0.1 rpm to monitor CD in the wavelength range of 200–800 nm to eliminate linear birefringence. Circular dichroism is defined as the difference in transmission of left- and right-handed circularly polarized light.<sup>[42]</sup>

## Supporting Information

Supporting Information is available from the Wiley Online Library or from the author.

## Acknowledgements

Z.C. and Y.M. contributed equally to this work. H.L.Z. acknowledges the financial Start-up support and Tier 1 support from Northeastern University. Y.M.L. acknowledges the financial support of National Science Foundation under grant number DMR-1654192. Z.C. would like to thank the China Scholarship Council (CSC) for its financial support. The authors thank the Kostas Research Institute at Northeastern University for the use of facilities. F.C. conducted the POM characterizations and analyzed the results. L.Y. and Z.F.H. conducted and analyzed part of the CD characterizations. Z.J.H. performed the UV-vis absorption and fluorescence spectroscopy measurements. All the authors contributed to writing the manuscript.

## Conflict of Interest

The authors declare no conflict of interest.

## Keywords

cellulose nanocrystals, chiral nematic structures, chiral plasmonic films, chiroptical activity, gold nanorod, surface-enhanced fluorescence

Received: December 27, 2018

Revised: January 25, 2019

Published online:

- [1] a) A. Kuzyk, R. Schreiber, Z. Fan, G. Pardatscher, E.-M. Roller, A. Högele, F. C. Simmel, A. O. Govorov, T. Liedl, *Nature* **2012**, 483, 311; b) A. Querejeta-Fernández, G. g. Chauve, M. Methot, J. Bouchard, E. Kumacheva, *J. Am. Chem. Soc.* **2014**, 136, 4788;

- c) X. T. Kong, L. V. Besteiro, Z. Wang, A. O. Govorov, *Adv. Mater.* **2018**, <https://doi.org/10.1002/adma.201801790>.
- [2] J. R. Mejía-Salazar, O. N. Oliveira, *Chem. Rev.* **2018**, *118*, 10617.
- [3] A. Querejeta-Fernández, B. Kopera, K. S. Prado, A. Klinkova, M. Methot, G. Chauve, J. Bouchard, A. S. Helmy, E. Kumacheva, *ACS Nano* **2015**, *9*, 10377.
- [4] A. V. Kabashin, P. Evans, S. Pastkovsky, W. Hendren, G. A. Wurtz, R. Atkinson, R. Pollard, V. A. Podolskiy, A. V. Zayats, *Nat. Mater.* **2009**, *8*, 867.
- [5] K. Sawai, R. Tatum, T. Nakahodo, H. Fujihara, *Angew. Chem.* **2008**, *120*, 7023.
- [6] A. Bobrovsky, K. Mochalov, V. Oleinikov, A. Sukhanova, A. Prudnikov, M. Artemyev, V. Shibaev, I. Nabiev, *Adv. Mater.* **2012**, *24*, 6216.
- [7] A. Klinkova, R. M. Choueiri, E. Kumacheva, *Chem. Soc. Rev.* **2014**, *43*, 3976.
- [8] a) J. C. Ndukaife, A. Mishra, U. Guler, A. G. A. Nnanna, S. T. Wereley, A. Boltasseva, *ACS Nano* **2014**, *8*, 9035; b) M. L. Brongersma, V. M. Shalaev, *Science* **2010**, *328*, 440.
- [9] a) E. Ringe, J. Zhang, M. R. Langille, K. Sohn, C. Cobley, L. Au, Y. Xia, C. A. Mirkin, J. Huang, L. D. Marks, R. P. Van Duyne, *MRS Proc.* **2009**, *1208*, 1208; b) M. Schlesinger, M. Giese, L. K. Blusch, W. Y. Hamad, M. J. MacLachlan, *Chem. Commun.* **2015**, *51*, 530.
- [10] V. K. Valev, J. J. Baumberg, C. Sabilia, T. Verbiest, *Adv. Mater.* **2013**, *25*, 2517.
- [11] A. M. Gabudean, M. Focsan, S. Astilean, *J. Phys. Chem. C* **2012**, *116*, 12240.
- [12] H. Wang, H. Li, S. Xu, B. Zhao, W. Xu, *Sci. Rep.* **2017**, *7*, 14630.
- [13] D. Darvill, A. Centeno, F. Xie, *Phys. Chem. Chem. Phys.* **2013**, *15*, 15709.
- [14] W. Wang, M. Ramezani, A. I. Väkeväinen, P. Törmä, J. G. Rivas, T. W. Odom, *Mater. Today* **2017**, *21*, 303.
- [15] F. Pineider, G. Campo, V. Bonanni, C. de Julián Fernández, G. Mattei, A. Caneschi, D. Gatteschi, C. Sangregorio, *Nano Lett.* **2013**, *13*, 4785.
- [16] a) Y. Fu, J. Zhang, J. R. Lakowicz, *J. Am. Chem. Soc.* **2010**, *132*, 5540; b) C. D. Geddes, J. R. Lakowicz, *J. Fluoresc.* **2002**, *12*, 121.
- [17] a) Q. Liu, Y. Cui, D. Gardner, X. Li, S. He, I. I. Smalyukh, *Nano Lett.* **2010**, *10*, 1347; b) Q. Liu, M. G. Campbell, J. S. Evans, I. I. Smalyukh, *Adv. Mater.* **2014**, *26*, 7178.
- [18] A. Lukach, H. I. Thérien-Aubin, A. Querejeta-Fernández, N. Pitch, G. g. Chauve, M. Méthot, J. Bouchard, E. Kumacheva, *Langmuir* **2015**, *31*, 5033.
- [19] a) G. Chu, G. Vasilyev, R. Vilensky, M. Boaz, R.-Y. Zhang, P. Martin, N. Dahan, S. Deng, E. Zussman, *Langmuir* **2018**, *34*, 13263; b) Y. Habibi, L. A. Lucia, O. J. Rojas, *Chem. Rev.* **2010**, *110*, 3479.
- [20] B. Frka-Petescic, H. Radavidson, B. Jean, L. Heux, *Adv. Mater.* **2017**, *29*, 1606208.
- [21] X. M. Dong, D. G. Gray, *Langmuir* **1997**, *13*, 2404.
- [22] G. Chu, X. Wang, H. Yin, Y. Shi, H. Jiang, T. Chen, J. Gao, D. Qu, Y. Xu, D. Ding, *ACS Appl. Mater. Interfaces* **2015**, *7*, 21797.
- [23] a) D. Qu, J. Zhang, G. Chu, H. Jiang, C. Wu, Y. Xu, J. Mater. Chem. C **2016**, *4*, 1764; b) K. E. Shopsowitz, H. Qi, W. Y. Hamad, M. J. MacLachlan, *Nature* **2010**, *468*, 422; c) K. E. Shopsowitz, W. Y. Hamad, M. J. MacLachlan, *Angew. Chem., Int. Ed.* **2011**, *50*, 10991.
- [24] J. A. Kelly, M. Giese, K. E. Shopsowitz, W. Y. Hamad, M. J. MacLachlan, *Acc. Chem. Res.* **2014**, *47*, 1088.
- [25] M. Giese, L. K. Blusch, M. K. Khan, M. J. MacLachlan, *Angew. Chem., Int. Ed.* **2015**, *54*, 2888.
- [26] J. P. Lagerwall, C. Schütz, M. Salajkova, J. Noh, J. H. Park, G. Scalia, L. Bergström, *NPG Asia Mater.* **2014**, *6*, e80.
- [27] K. Yao, Q. Meng, V. Bulone, Q. Zhou, *Adv. Mater.* **2017**, *29*, 1701323.
- [28] R. Bardet, N. Belgacem, J. Bras, *ACS Appl. Mater. Interfaces* **2015**, *7*, 4010.
- [29] A. G. Dumanli, H. M. van der Kooij, G. Kamita, E. Reisner, J. J. Baumberg, U. Steiner, S. Vignolini, *ACS Appl. Mater. Interfaces* **2014**, *6*, 12302.
- [30] H. Thérien-Aubin, A. Lukach, N. Pitch, E. Kumacheva, *Nanoscale* **2015**, *7*, 6612.
- [31] B. Frka-Petescic, G. Guidetti, G. Kamita, S. Vignolini, *Adv. Mater.* **2017**, *29*, 1701469.
- [32] P. Bharadwaj, B. Deutsch, L. Novotny, *Adv. Opt. Photonics* **2009**, *1*, 438.
- [33] P. Strobbia, E. R. Languirand, B. M. Cullum, *Opt. Eng.* **2015**, *54*, 100902.
- [34] J. Pérez-Juste, I. Pastoriza-Santos, L. M. Liz-Marzán, P. Mulvaney, *Coord. Chem. Rev.* **2005**, *249*, 1870.
- [35] a) B. Nikoobakht, M. A. El-Sayed, *Chem. Mater.* **2003**, *15*, 1957; b) T. Ye, Z. Dai, F. Mei, X. Zhang, Y. Zhou, J. Xu, W. Wu, X. Xiao, C. Jiang, *J. Phys.: Condens. Matter* **2016**, *28*, 434002.
- [36] H. Zheng, W. Li, W. Li, X. Wang, Z. Tang, S. X. A. Zhang, Y. Xu, *Adv. Mater.* **2018**, *30*, 1705948.
- [37] J. Liu, L. Yang, Z. Huang, *Small* **2016**, *12*, 5902.
- [38] a) R. Xiong, K. Hu, A. M. Grant, R. Ma, W. Xu, C. Lu, X. Zhang, V. V. Tsukruk, *Adv. Mater.* **2016**, *28*, 1501; b) H. Zhu, F. Shen, W. Luo, S. Zhu, M. Zhao, B. Natarajan, J. Dai, L. Zhou, X. Ji, R. S. Yassar, *Nano Energy* **2017**, *33*, 37.
- [39] A. Umar, S.-M. Choi, *J. Phys. Chem. C* **2013**, *117*, 11738.
- [40] a) N. R. Jana, L. Gearheart, C. J. Murphy, *J. Phys. Chem. B* **2001**, *105*, 4065; b) B. D. Busbee, S. O. Obare, C. J. Murphy, *Adv. Mater.* **2003**, *15*, 414.
- [41] W. Ni, Z. Yang, H. Chen, L. Li, J. Wang, *J. Am. Chem. Soc.* **2008**, *130*, 6692.
- [42] a) O. V. Surov, M. I. Voronova, A. G. Zakharov, *Russ. Chem. Rev.* **2017**, *86*, 907; b) C. D. Edgar, D. G. Gray, *Cellulose* **2001**, *8*, 5.